Detection of Rossby wave breaking and its response to shifts of the midlatitude jet with climate change

Elizabeth A. Barnes[1,2] and Dennis L. Hartmann[1]

Received 18 January 2012; revised 2 April 2012; accepted 3 April 2012; published 11 May 2012.

[1] A Rossby wave breaking identification method is presented which searches for overturning of absolute vorticity contours on pressure surfaces. The results are compared to those from an analysis of isentropic potential vorticity, and it is demonstrated that both yield similar wave breaking distributions. As absolute vorticity is easily obtained from most model output, we present wave breaking frequency distributions from the ERA-Interim data set, thirteen general circulation models (GCMs) and a barotropic model. We demonstrate that a poleward shift of the Southern Hemisphere midlatitude jet is accompanied by a decrease in poleward wave breaking in both the barotropic model and all GCMs across multiple climate forcing scenarios. In addition, it is shown that while anticyclonic wave breaking shifts poleward with the jet, cyclonic wave breaking shifts less than half as much and reaches a poleward limit near 60 degrees S. Comparison of the observed distribution of Southern Hemisphere wave breaking with those from the GCMs suggests that wave breaking on the poleward flank of the jet has already reached its poleward limit and will likely become less frequent if the jet migrates any further poleward with climate change.

Citation: Barnes, E. A., and D. L. Hartmann (2012), Detection of Rossby wave breaking and its response to shifts of the midlatitude jet with climate change, *J. Geophys. Res.*, *117*, D09117, doi:10.1029/2012JD017469.

1. Introduction

[2] Tropospheric mixing and transport in the middle and high latitudes are driven mainly by synoptic eddy activity. In many cases, these eddies grow by baroclinic instability and decay barotropically by breaking and inducing irreversible mixing of the surrounding air, termed "wave breaking" [*McIntyre and Palmer*, 1983]. Synoptic activity is important because it is associated with passing storms and because it plays a crucial role in the maintenance of the large-scale midlatitude jet streams [*Robinson*, 2006]. The Intergovernmental Panel on Climate Change Fourth Assessment Report found that global circulation models (GCMs) predict a robust poleward shift of the midlatitude, eddy-driven jets in both hemispheres in response to increased greenhouse gas (GHG) forcing [*Meehl et al.*, 2007b]. Due to the strong coupling between synoptic eddy activity and the jet streams, a poleward shift of the jet implies a shift in eddy activity as well, although separating cause and effect is not trivial.

[3] Rossby waves preferentially propagate equatorward, an effect easily seen from climatological E-P flux diagnostics [*Edmon et al.*, 1980]. *Hoskins et al.* [1977] attribute this phenomenon to the fact that midlatitude waves preferentially *propagate* equatorward due to spherical geometry. However, *Nakamura and Plumb* [1994] demonstrate that preferential equatorward wave *breaking* requires only an asymmetry in the meridional shear on each side of the jet, which causes the critical line on the equatorward flank to be nearer the jet than the critical line on the poleward flank. In either case, both mechanisms lead to preferential equatorward Rossby wave propagation and dissipation.

[4] Recent work by *Barnes et al.* [2010] and *Barnes and Hartmann* [2011] suggest that an important implication of a poleward shift of the jet is a reduction in wave breaking on the poleward flank of the jet. They argue that the critical line on the poleward flank of the jet vanishes due to the decrease in the background vorticity gradient if the jet moves far enough poleward. This results in increased equatorward wave propagation and wave breaking in the subtropics. They demonstrated that this change in eddy activity can explain the reduction in the persistence of the annular modes in climate change simulations. However, the inferences in these studies were based upon linear wave theory and did not quantify the actual changes in wave breaking associated with a poleward shift of the jet. In the following sections, we will introduce a wave breaking detection algorithm and use it to investigate the response of wave breaking frequency to

[1]Department of Atmospheric Science, University of Washington, Seattle, Washington, USA.
[2]Now at Lamont-Doherty Earth Observatory, Columbia University, Palisades, New York, USA.

Corresponding author: E. A. Barnes, Lamont-Doherty Earth Observatory, Columbia University, PO Box 1000, Palisades, NY 10964, USA. (eabarnes@ldeo.columbia.edu)

0148-0227/12/2012JD017469

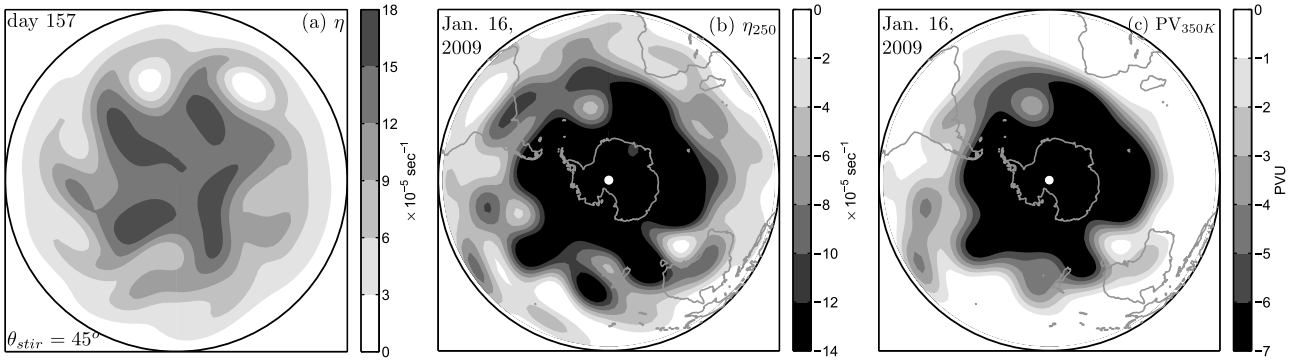

Figure 1. Snapshots of instantaneous fields of (a) absolute vorticity in the barotropic model, and ERA-Interim (b) 250 hPa absolute vorticity and (c) potential vorticity on the 350 K potential temperature surface. Figures 1b and 1c have been smoothed as outlined in Section 2.2.

increased greenhouse gas forcing and a poleward shift of the eddy-driven jet.

2. Methods

2.1. Data

2.1.1. Barotropic Model

[5] Instantaneous daily zonal wind (u), meridional wind (v) and relative vorticity (ζ) are obtained from a nonlinear barotropic model on the sphere. Variations of this particular barotropic model setup have been documented in the recent literature [*Vallis et al.*, 2004; *Barnes et al.*, 2010; *Barnes and Hartmann*, 2011], but we repeat details here for completeness. The model integrates

$$\frac{\partial \zeta}{\partial t} + \frac{u}{a\cos\theta}\frac{\partial \zeta}{\partial \lambda} + \frac{v}{a}\frac{\partial \zeta}{\partial \theta} + v\beta = \mathcal{S} - r\zeta - \kappa\nabla^4\zeta, \qquad (1)$$

where r is the damping parameter set equal to 1/6 days^{-1} and κ is the diffusion coefficient for parameterizing the removal of enstrophy at small scales. We model the stirring of the atmosphere by baroclinic eddies as an Ornstein-Uhlenbeck stochastic process ($\mathcal{S}$) defined for each combination of total wave number l and zonal wave number m:

$$\mathcal{S}^i_{lm} = (1 - e^{-2dt/\tau})^{1/2}\mathcal{Q}^i + e^{-dt/\tau}\mathcal{S}^{i-1}_{lm}, \qquad (2)$$

where i is the time step index, τ denotes the decorrelation time of the stirring (2 days) and dt is the model time step (3600 sec). $\mathcal{Q}^i$ is a real number chosen uniformly between $(-\mathcal{A}, \mathcal{A}) \times 10^{-11}$, where $\mathcal{A}$ is the stirring strength (see *Vallis et al.* [2004] for details) set equal to 7.0 for this work. The model is stirred between total wave numbers 8 and 12, with the minimum zonal wave number equal to 4 so that the zonal-mean flow is not forced directly. A meridionally confined storm track is created from this global stirring by windowing the gridded stirring field with a Gaussian spatial mask centered at latitude θ_{stir} with a half-width of 12°. The model is run at T42 resolution and each integration is spun-up for 500 days before being integrated another 4000 days for analysis.

[6] Figure 1a shows the absolute vorticity field on day 157 for the integration with stirring centered at 45°N. The field is relatively smooth since we are only stirring at synoptic wave numbers (rather than over the range of all possible scales). The large gradient in absolute vorticity in midlatitudes is evidence of an eddy-driven jet, and the wave like behavior of the contours is clearly evident. We will compare the wave breaking behavior of this model with that of GCMs and the observations in the coming sections.

2.1.2. ERA-Interim

[7] For the observational portion of this work, we use over 22 years (Jan. 1, 1989–Apr. 30, 2011) of latitude-longitude gridded daily (1200 UTC) u, v and ζ on 20 pressure levels (10–925 hPa) from the ERA-Interim data set produced by the European Centre for Medium Range Weather Forecasts (ECMWF) [*Simmons et al.*, 2006]. In addition, we use gridded potential vorticity on the 16 potential temperature surfaces (265–850 K) provided. In this work, we define daily anomalies at a single grid point as departures from the mean seasonal cycle, computed as the mean plus the first four Fourier harmonics of the daily climatology over the entire period.

2.1.3. General Circulation Models

[8] We analyze 13 general circulation models (GCMs) to quantify changes in wave breaking associated with increased greenhouse gas forcing. We use three scenarios archived by the World Climate Research Programme's (WCRP's) Coupled Model Intercomparison Project Phase 3 (CMIP3) [*Meehl et al.*, 2007a]: the 20C3M scenario (1961–2000; 40 years), A2 scenario (2081–2100; 20 years) and the 2 × CO_2 scenario (20 years). Relative vorticity was not archived for these models, so instead we use u and v to calculate the relative vorticity as $\zeta = \nabla \times \mathbf{u}$, where $\mathbf{u} = (u, v)$. We analyze only the pressure surface nearest to 250 hPa for eleven of the GCMs (most models output 300 hPa), and present the wave breaking climatology of the GFDL CM2.0 GCM [*Delworth et al.*, 2006] at all output pressure levels for additional detail.

2.2. Smoothing of Fields

[9] The ERA-Interim and GCM fields are smoothed before the wave breaking algorithm is applied to ensure that the detection method only identifies large-scale overturning as a wave breaking event, rather than small-scale perturbations in the field. This is accomplished by expanding in spherical harmonics to T42 and then truncating at T15. We have tested this smoothing technique and note that truncating at T20 produces similar wave breaking

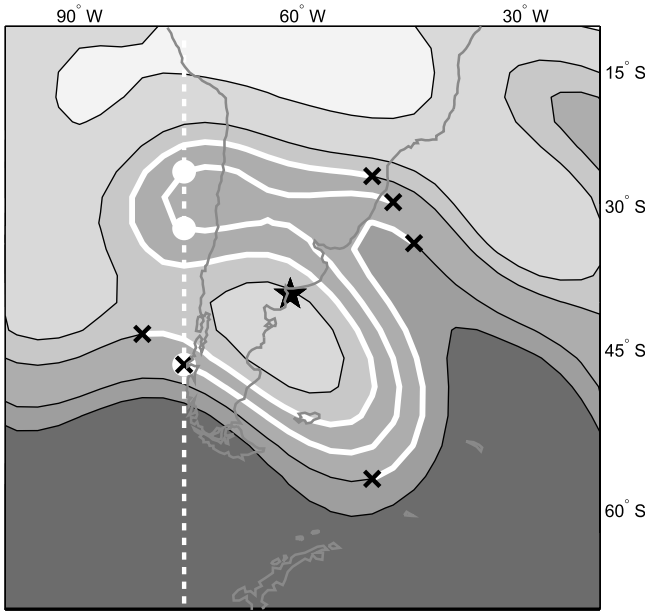

Figure 2. Detection of a wave breaking event on the 250 hPa absolute vorticity surface. The dashed white line denotes a meridian that intersects a contour at three *overturning points* which are denoted by closed white circles. The solid white contours connect all such overturning points. The black crosses denote each contour's west-most and east-most overturning points used to determine breaking orientation, and the black star denotes the centroid of the wave breaking event.

frequencies. This smoothing is not performed in the barotropic model as the fields are already smoothed by the fact that we are only stirring at synoptic scales. However, we have verified that the barotropic results are robust when the fields are smoothed in this manner.

[10] All zonally integrated profiles of wave breaking are binned in increments of 2° latitude. The single latitude profiles are smoothed with a 1-2-1 filter to aid in visualization. Unsmoothed fields were used to make the pressure-latitude plots in order to retain more of the details in the distribution. The conclusions are the same whether or not smoothing is performed.

2.3. Wave Breaking Detection Algorithm

[11] The goal of this work is to identify large-scale wave breaking in gridded data sets and quantify the response of wave breaking frequency to climate change. We use the phrase "large scale" to refer to synoptic scales larger than approximately 1000 km. Figures 1b and 1c depict example wave breaking events of the absolute vorticity field ($\eta \equiv f + \zeta$, where f is the Coriolis parameter) on the 250 hPa surface in the reanalysis as well as the potential vorticity field on the 350 K potential temperature surface. Both fields show wave-like behavior with clear evidence of overturning off the southern coast of Australia. In the coming sections we will compare wave breaking frequencies of absolute and potential vorticity and show that similar distributions are obtained.

[12] We begin by describing the wave breaking detection algorithm using a dynamical field of interest $\mathcal{X}$. Each day, we search for large-scale wave breaking on $\mathcal{X}$ by searching for regions of overturning of the contours. Figure 2 shows an example of a wave breaking event in the 250 hPa absolute vorticity field from the reanalysis. The algorithm identifies wave breaking events by first defining $\mathcal{C}$ as the longest closed contour of a certain value that encircles the pole. Note that the grid spacing of $\mathcal{C}$ will be higher resolution than the original data grid because the contouring procedure uses linear interpolation. Upon calculating the contour, the algorithm searches for locations where a single meridian (white dashed line in Figure 2) intersects $\mathcal{C}$ at least three times. When this occurs, we call these three intersection grid points *overturning points* for this contour and meridian, and three such points are denoted as white circles in Figure 2. The white solid lines in Figure 2 connect all such overturning points on three neighboring absolute vorticity contours.

[13] Overturning points within 500 km of each other along the contour are considered part of the same event and are grouped together. The algorithm is robust to this parameter and was chosen by inspecting many events and ensuring that distant overturning events were not erroneously grouped together. The amount of overturning required is specified by the minimum longitudinal width of the overturning event, which is set here to 5°. This parameter is given in units of degrees and not distance to ensure that wave breaking events near the pole are not missed by the algorithm due to the decrease in contour length with latitude. This method is applied daily to a range of contour values with all resulting overturning groups saved.

[14] The next step groups the overturning contours into daily wave breaking events. It is clear in Figure 2 that all three white contours are a part of the same anticyclonic wave breaking event. The algorithm groups these overturning contours into a single day's wave breaking event by searching for contiguous contours that all have overturning with centers within 2000 km of each other, where the centers are the geographic centers of the overturning points. If this criterion is not fulfilled, the overturning contours are considered different wave breaking events. We define the center of a wave breaking event as the geographic center of all grid points on all contours in the event. The center of the wave breaking event in Figure 2 is denoted by a black star, and is the location used to define all spatial wave breaking statistics in this work.

[15] The results presented here focus on the orientation of the wave breaking events, where we split the events into those that overturn cyclonically and those that overturn anticyclonically. To do this, we order the overturning points from west to east along the contour. In the Southern Hemisphere, cyclonic wave breaking events are defined as those whose west-most overturning point is equatorward of the east-most overturning point and anticyclonic wave breaking events are defined as those whose west-most overturning point is poleward of the east-most overturning point. The naming conventions are opposite in the Northern Hemisphere. The west-most and east-most points used to determine wave breaking orientation are denoted as black crosses in Figure 2.

[16] A single wave breaking event often lasts more than one day. In order to ensure that we do not double count the

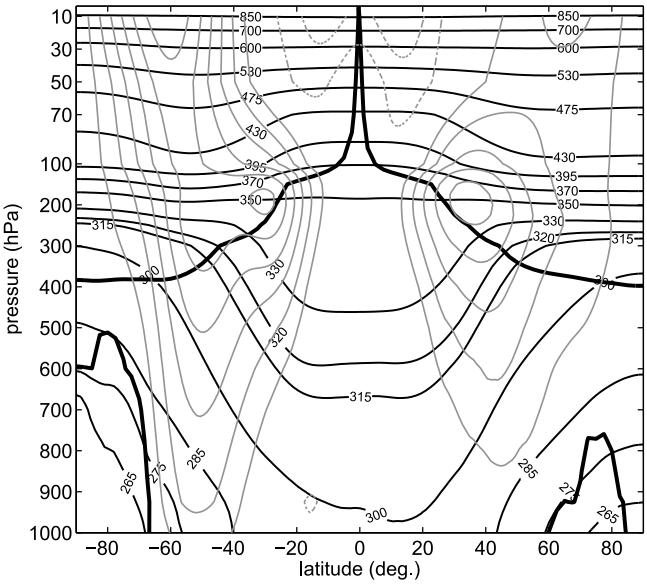

Figure 3. Annual-mean zonally averaged zonal winds (gray contours), potential temperature (labeled black contours) and the 2 PVU potential vorticity surface (thick black contour) from ERA-Interim Reanalysis. Dashed gray lines denote easterlies. The linear vertical spacing changes at 100 hPa to highlight the stratosphere.

same wave breaking event across multiple days, the final step groups wave breaking events in time that have centers within 2000 km of each other. The first day of the group is defined as the "onset day". In ERA-Interim, the median wave breaking event persistence at 250 hPa is 2 days. While this analysis only utilizes statistics for the onset day, the qualitative features of the frequency distributions are similar for all fields if all days of a wave breaking event are used. This result confirms that the analysis is robust with respect to the temporal grouping of the wave breaking events.

2.4. Diagnostic Fields

[17] In the following sections, we present results for absolute vorticity on pressure surfaces and look for wave breaking on 20 absolute vorticity contours $\pm[1, 2, \ldots, 4.18] \times 10^{-5}$ sec^{-1}. These contours range over the globe and are used for analysis of the barotropic model, reanalysis and the GCMs. For reference, Figure 3 depicts the annual-mean zonal-mean zonal winds from ERA-Interim along with climatological potential temperature surfaces and the 2 PVU surface.

[18] Several previous studies have identified wave breaking using isentropic potential vorticity. Isentropic potential vorticity is often considered the ideal field to search for wave breaking because it is conserved under adiabatic flow and thus can be viewed as a material tracer. Some authors have identified wave breaking of the dynamic tropopause (2 PVU contour where 1 PVU unit = $10^{-6} \cdot \mathrm{K} \cdot \mathrm{m}^2 \cdot \mathrm{kg}^{-1}\mathrm{s}^{-1}$) on various potential temperature surfaces [*Wernli and Sprenger*, 2007; *Martius et al.*, 2007; *Isotta et al.*, 2008] while others extend their search to the 1.5, 2.0 and 2.5 PVU contours [*Ndarana and Waugh*, 2011]. Additional studies identify wave breaking across 40 different contours, in increments of 0.5 PVU [*Strong and Magnusdottir*, 2008; *Wang and Magnusdottir*, 2011] and we use a similar contouring here. Specifically, we search for wave breaking on 40 contours $\pm[0.3, 0.8, \ldots, 9.8]$ PVU in increments of 0.5 PVU.

[19] We will demonstrate that wave breaking frequencies calculated using isobaric absolute vorticity are similar to those calculated using isentropic potential vorticity. Ignoring diabatic effects, isobaric potential vorticity and isobaric absolute vorticity differ in that isobaric PV includes a stretching term to account for divergence of the flow and thus vorticity sources and sinks. Away from regions of strong baroclinicity, Rossby-wave propagation is barotropic in nature, making the stretching of vorticity less important. For this reason, we may expect isobaric potential and absolute vorticity to largely agree. In regions where the isobars are parallel to the isentropes, isobaric and isentropic potential vorticity will be similar. Thus, we might expect at large scales, and away from regions of strong baroclinicity, isentropic potential vorticity and isobaric absolute vorticity will behave similarly.

2.5. Summary of Wave Breaking Detection Algorithm

[20] Several wave breaking detection algorithms exist in the literature, so it is relevant to ask whether this one is needed. We are interested in detecting wave breaking at all latitudes, and algorithms that search for overturning on only one or two contours are unable to provide such coverage. In addition, some previous studies count wave breaking on every contour as a unique event [*Ndarana and Waugh*, 2011], or consider all overturning points from a single wave breaking event to contribute to the total wave breaking frequency [*Hitchman and Huesmann*, 2007; *Rivière et al.*, 2010; *Rivière*, 2011]. In both cases, changes in contour spacing will immediately modify the number of wave breaking events identified. In addition, events that span a larger spatial range will be more heavily weighted. While in some studies these properties may be preferred, here we are interested in the absolute count of wave breaking events and how it varies with the jet. The algorithm presented here groups neighboring overturning contours into a single event, and thus counts both large and small events equally and is robust to contour spacing.

[21] Wave breaking statistics for absolute and potential vorticity will be presented in subsequent sections. As previously mentioned, isentropic potential vorticity is most often used to detect wave breaking. However, to our knowledge, *Rivière* [2009], *Rivière et al.* [2010] and *Rivière* [2011] are the only studies that have used isobaric absolute vorticity, and they analyzed only a single pressure level and made no comparison with isentropic absolute vorticity. We will demonstrate that the absolute vorticity field is suitable for quantifying large-scale wave breaking in the upper-troposphere and compares well with meridional wave breaking statistics computed from isentropic potential vorticity. In addition, isobaric absolute vorticity can unambiguously capture the entire meridional distribution of wave breaking and can easily be calculated from most model output.

3. Wave Breaking in a Barotropic Model

3.1. Varying θ_{stir}

[22] We begin by analyzing the effect of jet latitude on Rossby wave breaking frequency in a stirred barotropic model (see Section 2 for model setup). We vary the eddy-

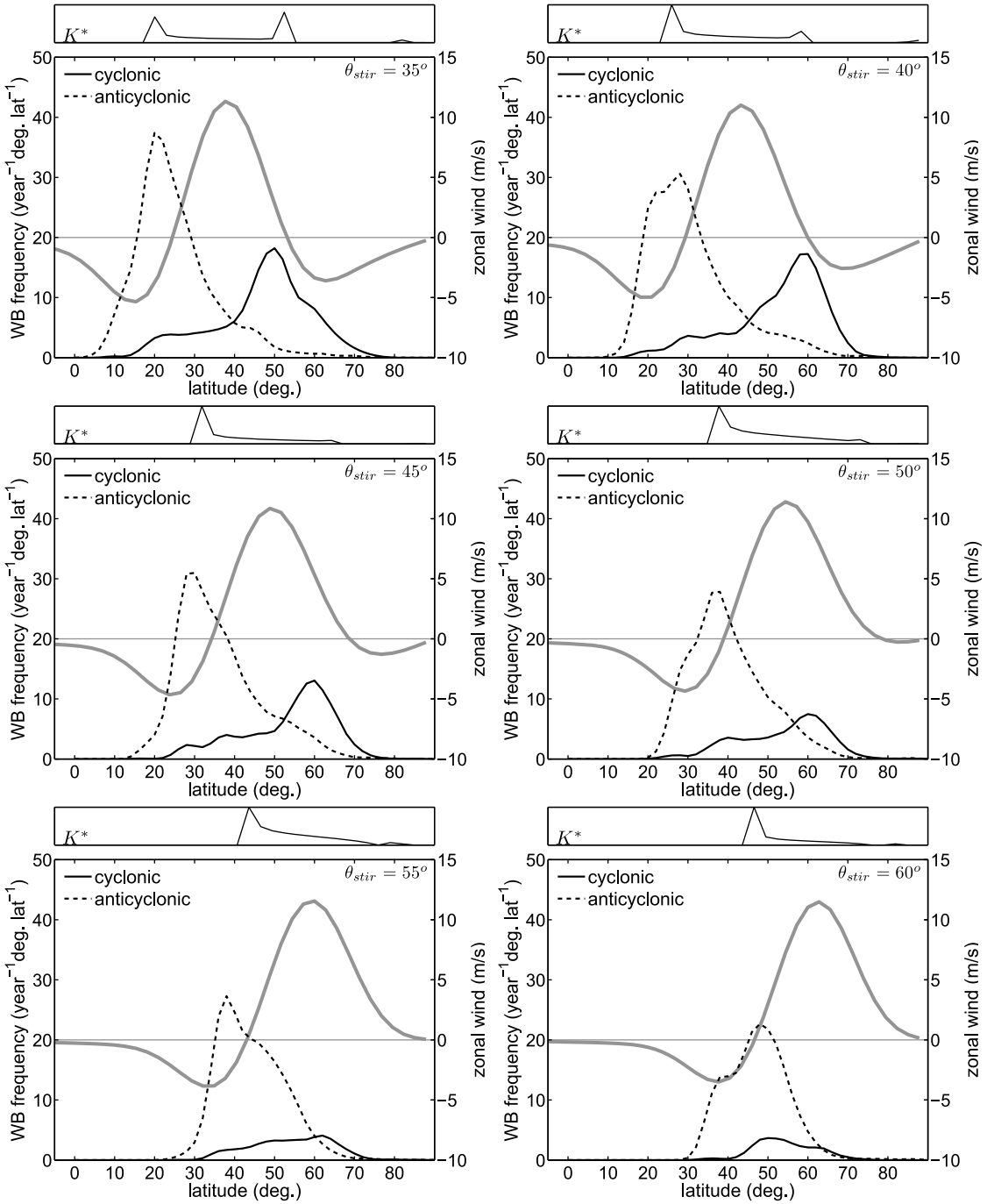

Figure 4. Wave breaking frequency versus latitude in the barotropic model where the stirring latitude is varied. Black solid lines denote cyclonic wave breaking events and black dashed lines denote anticyclonic events. The thick gray curve denotes the zonal-mean zonal wind with the axes on the right-hand side. K^* is plotted at the top of each panel for the power-weighted phase speed at the latitude of the jet.

driven jet latitude by moving the latitude of stirring, θ_{stir} in 5° increments between 10°N and 70°N. A selection of the resulting wave breaking frequency distributions is shown in Figure 4. The frequencies are displayed as the number of unique events per 365-day year per degree latitude to make the results independent of the grid spacing. The gray curves denote the zonal-mean zonal wind for each integration, with axes on the right-hand-side of each panel.

[23] Focusing on the θ_{stir} = 35°N case, anticyclonic wave breaking events tend to occur equatorward of the jet (on the anticyclonically sheared flank) while cyclonic events appear predominantly poleward of the jet (on the cyclonically sheared flank), a characteristic of wave breaking that has been noted by many previous authors [*Thorncroft et al.*, 1993; *Nakamura and Plumb*, 1994; *Peters and Waugh*, 1996]. Note that cyclonic wave breaking also occurs on the

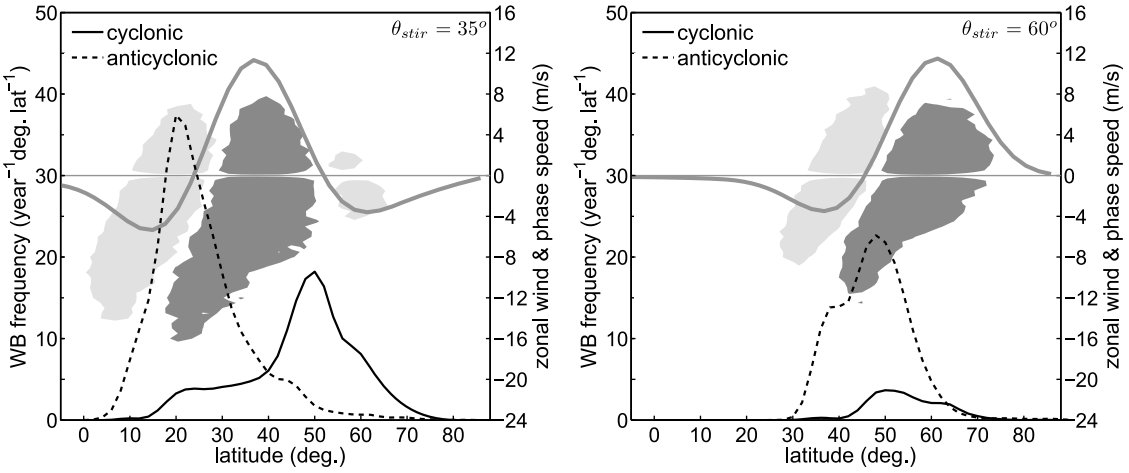

Figure 5. Shaded contours of $\cos(\theta) \times D_\theta$ versus phase speed and latitude contoured at $\pm 2 \times 10^{-7}$ m·sec^{-2} for θ_{stir} = 35°N and θ_{stir} = 60°N. Black dashed curves denote anticyclonic wave breaking frequency and black solid curves denote cyclonic wave breaking frequency. The gray curve denotes the zonal-mean zonal wind with axes on the right-hand-side of each panel.

equatorward flank of the jet, a result that may first appear counterintuitive due to the anticyclonic shear there. We have confirmed that this is not an artifact of zonal or temporal averaging, but rather, it is due to strong southeasterly flow with weaker winds to the west of this flow (in the Northern Hemisphere) which together induce cyclonic overturning of the vorticity contours. We have confirmed that cyclonic wave breaking in subtropical anticyclonic shear occurs only when strong easterlies are present and will discuss additional evidence of this feature in the observations in a later section.

[24] In all integrations, anticyclonic wave breaking is more frequent than cyclonic wave breaking. As mentioned in the Introduction, both wave propagation on the sphere and differences in cross-jet shear and proximity of the critical lines have been cited to explain this effect. In either case, both would predict more anticyclonic than cyclonic events, and this is indeed what we see here.

[25] By inspection of Figure 4, it is clear that as the jet shifts poleward, the number of cyclonic wave breaking events decreases, and to a lesser extent, the number of anticyclonic wave breaking events also decreases. *Barnes et al.* [2010] and *Barnes and Hartmann* [2011] argue that wave breaking on the poleward flank of the jet is expected to become less frequent as the jet shifts poleward due to the decrease in β toward the pole brought about by the spherical geometry of the earth. Specifically, they use a linear diagnostic related to the index of refraction, the wave number K^*, defined as

$$K^* = \cos\theta \left(\frac{\hat{\beta}}{\overline{u} - c} \right)^{1/2}, \tag{3}$$

where $\hat{\beta}$ is the meridional gradient of absolute vorticity and c is the phase speed of the wave. The factor of cosine accounts for the fact that the wave number k associated with a particular length scale decreases with latitude. A propagating wave with wave number k turns when it reaches the latitude where $K^* = k$ and propagates toward its critical latitude where the phase speed approaches $\overline{u}$ and K^* is large [*Hoskins and Karoly*, 1981; *Held*, 1983]. The argument is that as the jet moves poleward, the small value of β causes K^* to go to zero, and thus waves are unlikely to break on the poleward flank of the jet. Instead, they turn and propagate equatorward, breaking at the equatorward critical line at lower latitudes.

[26] One may criticize the use of the linear diagnostic K^* to diagnose wave breaking, which is a nonlinear process. To show that K^* does indeed provide information about the location of wave breaking, we plot K^* above each panel in Figure 4. The phase speed used to define K^* is the power-weighted phase speed of the eddy-momentum flux convergence at the latitude of the jet calculated using the method of *Randel and Held* [1991]. Theory predicts that wave breaking will occur where K^* is large, and indeed, the peaks in K^* align nearly perfectly with the locations of maximum wave breaking. As the mean jet moves poleward with the stirring, the poleward wave breaking decreases as predicted by K^*, and both go to zero at high latitudes.

[27] To demonstrate the effect of the wave breaking on the momentum budget, we compute the divergence of the y-component of the Eliassen-Palm flux [*Edmon et al.*, 1980]

$$D_\theta = \frac{1}{a\cos^2\theta} \frac{\partial}{\partial\theta} \left(-\overline{u'v'} \cos^2\theta \right) \tag{4}$$

in phase speed-latitude space following the method of Randel and Held [1991]. The resulting spectra for the θ_{stir} = 35°N and θ_{stir} = 60°N are shown in Figure 5. The dark and light shading show the regions of eddy momentum flux convergence and divergence respectively, multiplied by the cosine of latitude to highlight the torque felt by the mean flow. These regions align well with the regions of wave breaking, and as the wave breaking on the poleward flank vanishes, so too does the eddy momentum flux divergence.

[28] Figure 6a shows the global wave breaking frequency versus jet latitude for the barotropic integrations, where the latitude of the jet is defined as the latitude of maximum zonal-mean zonal winds. For the barotropic integrations with stirring near the equator, the equatorward lobe of wave

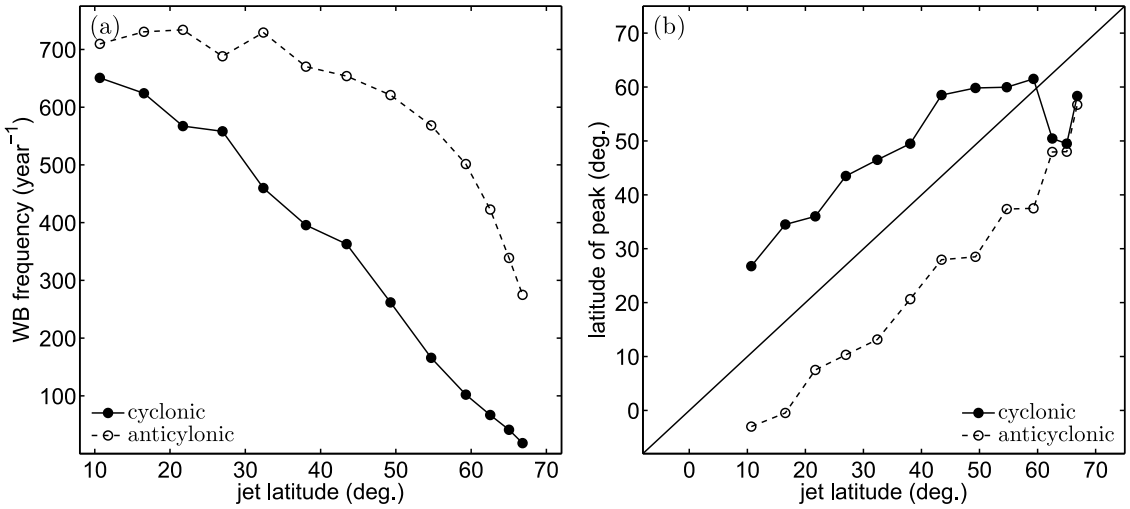

Figure 6. (a) Wave breaking frequency and (b) latitude of maximum wave breaking versus the latitude of the eddy-driven jet in the barotropic model separated into cyclonic and anticyclonic events (see text for note on classifications near the equator).

breaking occurs in the Southern Hemisphere, where counterclockwise rotation would be termed "cyclonic". To make the figure more clear, and demonstrate the changes in frequency of wave breaking southward of the jet, we have kept the Northern Hemisphere cyclonic and anticyclonic naming conventions for this figure only. The observed decrease in wave breaking with latitude is clear in Figure 6a, with the cyclonic events decreasing to zero as the jet moves poleward. The anticyclonic wave breaking events do not respond as quickly to the decrease in β since they are situated on the equatorward flank of the jet. However, once the jet is located near 40°N anticyclonic wave breaking frequency begins to decrease as well. This decrease in wave breaking as the jet moves poleward is due to the fact that only small wave numbers (large waves) can propagate in regions of small β. Thus, the decrease in wave breaking is also a function of stirring scale. We have confirmed that stirring over smaller wave numbers (larger scales) results in a less rapid decrease in wave breaking although the results are qualitatively similar.

[29] One might expect that as the jet shifts poleward, the regions of wave breaking will shift poleward with the winds. Looking at Figure 4, a poleward shift of the jet gives rise to a poleward shift of the peak in anticyclonic wave breaking. The peak in cyclonic wave breaking also shifts poleward for θ_{stir} between 35°N and 40°N. However, this does not continue for more poleward jet shifts. Figure 6b depicts the latitude of the maximum cyclonic and anticyclonic wave breaking frequency for varying stirring latitudes. Recalling that anticyclonic events occur predominantly equatorward of the jet, we see that the frequency distribution of these events shifts linearly with the latitude of the jet, parallel to the one-to-one line. The cyclonic events, however, slow their poleward progression when the jet is poleward of 40°N. It appears that the waves are unable to propagate and break any further poleward than 60°N, and when the jet latitude coincides with this latitude, the peak in cyclonic events moves to the equatorward flank of the jet, becoming collocated with the peak in anticyclonic events. Investigation of Figure 4 shows that cyclonic wave breaking does not actually increase on the equatorward flank of the jet for $\theta_{stir} \geq 60°$N, but rather decreases to zero on the poleward flank.

3.2. Adding a Subtropical Jet

[30] Thus far, we have analyzed wave breaking in a barotropic model with only a single eddy-driven jet. However, in the observations, there exists a strong subtropical jet between 20°N–30°N in both hemispheres, as shown for the zonal-mean in Figure 3. *Barnes and Hartmann* [2011] argue that the presence of a strong subtropical jet can greatly influence the variability of the midlatitude eddy-driven jet by modulating the latitude of wave breaking, thereby decreasing the positive feedback between the eddies and the eddy-driven jet.

[31] We design an experiment similar to *Barnes and Hartmann* [2011] whereby a fixed subtropical jet is added to the barotropic model simulations, and we refer the reader there for additional details and a comprehensive discussion of the eddy response. The subtropical jet is modeled as a Gaussian in latitude, centered at 30°N with a half-width of 6° and a maximum speed of 25 m·s^{-1}. The vorticity in the subtropics is relaxed back to this profile with a timescale of 6 days.

[32] We once again stir the model to create an eddy-driven jet that varies in space and time. We evaluate the wave breaking for the θ_{stir} = 50°N integration to mimic the Southern Hemisphere winter-time Pacific; the results are shown in Figure 7a. The gray solid line denotes the total zonal-mean zonal winds and is a combination of the imposed subtropical and eddy-driven winds. The gray dashed line denotes the eddy-driven jet, which is the component of the zonal-mean zonal winds driven purely by eddies, calculated as the total zonal winds minus the imposed Gaussian subtropical jet profile. Note that although the subtropical jet is relaxed to 25 m·s^{-1}, the eddies maintain it at a speed much less than this.

[33] The frequency distributions of anticyclonic (black dashed line) and cyclonic wave breaking (black solid line) in

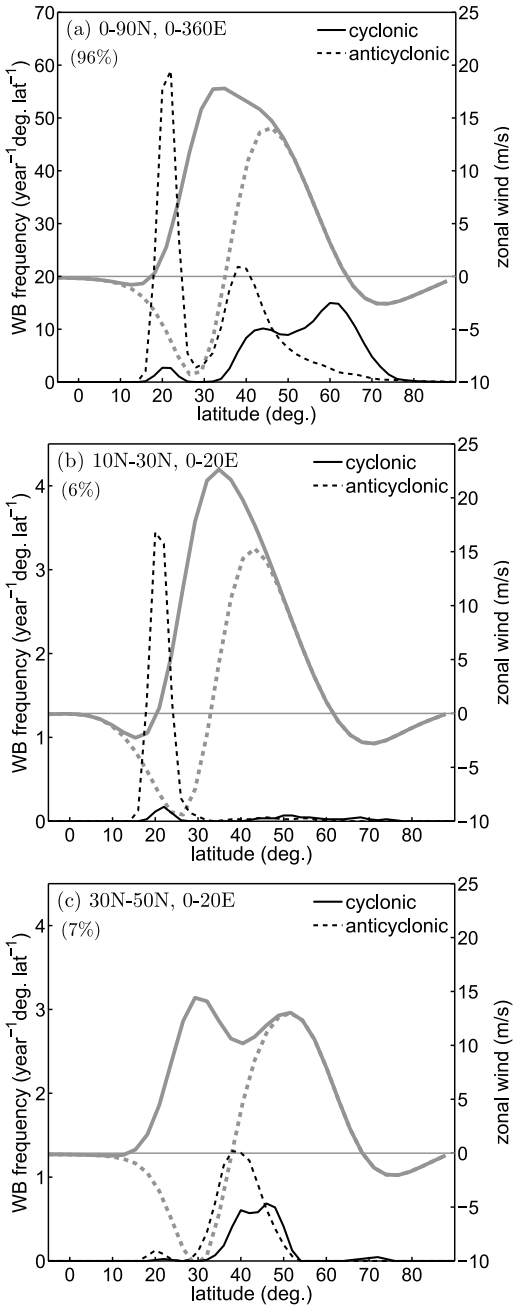

Figure 7. Wave breaking frequency versus latitude in the barotropic model for θ_{stir} = 50°N with a fixed subtropical jet centered at 30°N. Frequencies are composited on days when there is a wave breaking event in (a) the hemisphere, (b) the sector 10°N–30°N, 0°–20°E, and (c) the sector 30°N–50°N, 0°–20°E. Black solid lines denote cyclonic wave breaking events and black dashed lines denote anticyclonic events. The gray solid curve denotes the total zonal-mean zonal wind in the specified sector composited on days when there is wave breaking there. The gray dashed curve denotes the eddy-driven component of the zonal winds. The percentage of days with wave breaking in the specified sector is shown in the upper-left-hand corner of each panel.

Figure 7a differ significantly from the case without a subtropical jet (Figure 4). Whereas anticyclonic wave breaking peaked at 30°N in the single jet case, the presence of the subtropical jet causes a double-peak in anticyclonic wave breaking. However, from Figure 7a alone, it is unclear whether the double-peaked distribution of wave breaking represents wave breaking at these latitudes at the same time, or whether it is an artifact of zonal and temporal averaging. To obtain a clearer picture, we composite the zonal winds and the wave breaking frequencies on days when there is a wave breaking event between 0°–20°E on the subtropical flank of the jet (Figure 7b) and on days when there is a wave breaking event in the midlatitudes (Figure 7c). Figure 7b demonstrates that when there is a wave breaking event on the equatorward flank of the subtropical winds the two jets are merged together. Figure 7c demonstrates that when there is a wave breaking event in the midlatitudes (30°N–50°N), the two jets are separated, with the eddy-driven winds setting the critical line. These composites highlight the fact that the double-peaked wave breaking distribution in the time mean is due to temporal averaging over two flow regimes: (1) a merged jet state and (2) a separated jet state.

4. Wave Breaking in ERA-Interim

[34] Our method of diagnosing wave breaking facilitates the analysis of wave breaking on multiple pressure levels which can produce wave breaking distributions in all three dimensions and in time. We have identified large-scale overturning between levels ranging from 10 hPa to 925 hPa in ERA-Interim, where we treat every pressure level independently and apply the wave breaking algorithm to the absolute vorticity field on each surface.

4.1. Wave Breaking Frequency Profiles

[35] Figures 8a and 8b show the pressure-latitude distribution of wave breaking frequency in JJA and DJF. As previously discussed, during the Southern Hemisphere winter, the zonal-mean zonal winds exhibit a strong subtropical jet. Consistent with the subtropical winds influencing the latitudes of wave breaking, the vertical profile shown in Figure 8a exhibits a maximum in wave breaking frequency on the equatorward flank of this jet throughout the mid- and upper-troposphere. Recall that each pressure level is analyzed independently, so a single wave breaking event that extends throughout multiple levels will be counted at each level. It is interesting how the tropical wave breaking that must exist to support the Hadley cell momentum budget occurs in a narrow region on the equatorward flank of the subtropical jet and thus supports the sharpness of the jet there. A secondary maximum in wave breaking occurs in the midlatitudes on the equatorward flank of the barotropic component of the zonal winds (flank of the eddy-driven jet). These features are also evident in the Northern Hemisphere winter in DJF although the signal is less clear. Wave breaking is most frequently observed in the upper troposphere, but rarely extends above 100 hPa. However, in the winter-time stratosphere, a local maximum in wave breaking occurs along the flank of the polar vortex, a feature that has been extensively studied by previous authors using observed

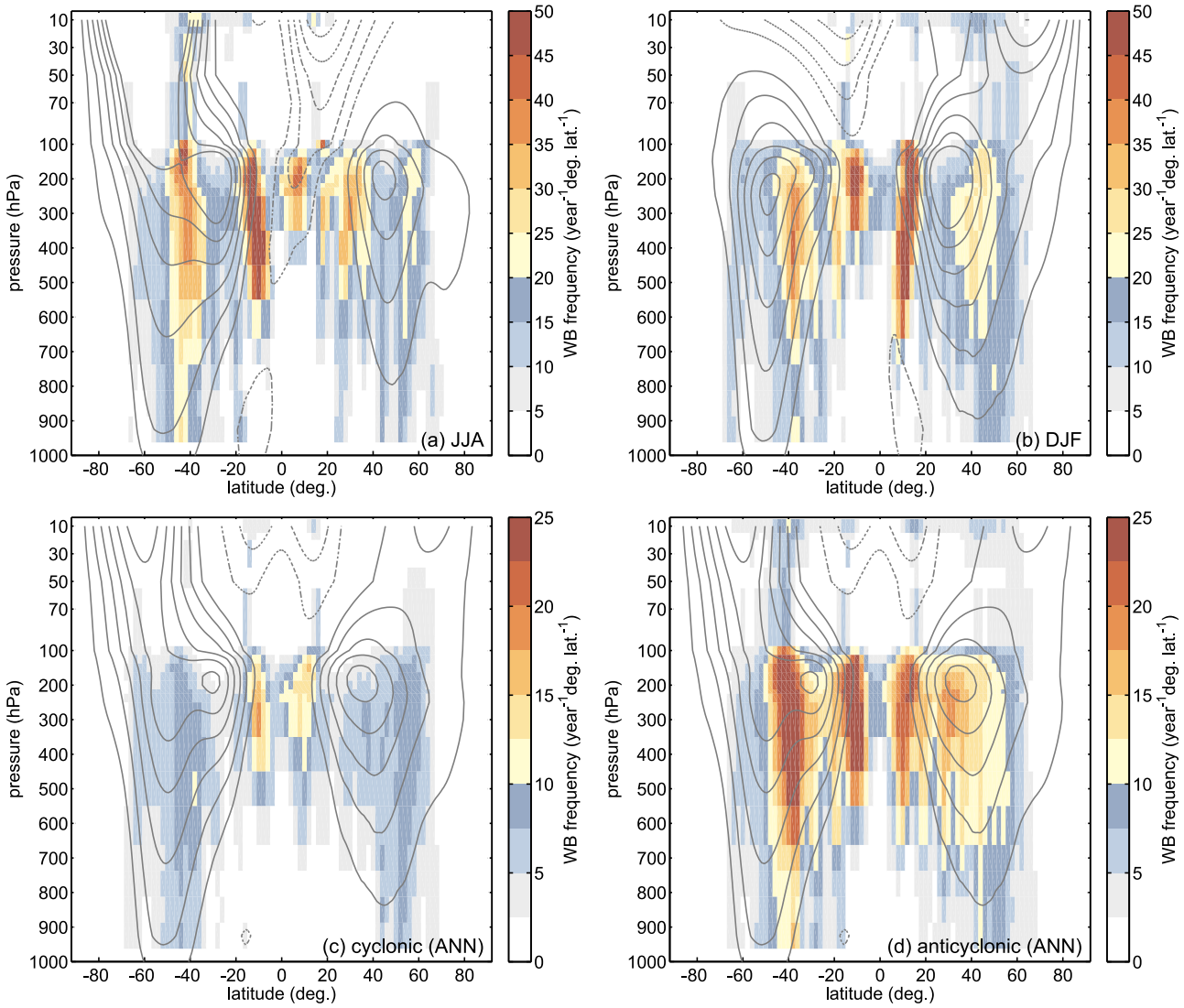

Figure 8. Zonally integrated wave breaking frequency for the ERA-Interim Reanalysis during (a) JJA and (b) DJF and in the annual-mean for (c) cyclonic and (d) anticyclonic orientations. Zonal-mean zonal winds are contoured every 5 m/s in gray, with the zero line omitted. Dashed gray lines denote easterlies, and the linear vertical spacing changes at 100 hPa to highlight the stratosphere.

potential vorticity [*McIntyre and Palmer*, 1983; *Baldwin and Holton*, 1988; *Abatzoglou and Magnusdottir*, 2007].

[36] Figures 8c and 8d display annual mean wave breaking frequencies decomposed into cyclonic and anticyclonic events (note the change in contour intervals compared to Figures 8a and 8b). Anticyclonic wave breaking is more frequent than cyclonic wave breaking and is found predominantly on the flanks of the jets and extends into the stratosphere. Cyclonic breaking tends to be spread over a wide range of latitudes and also occurs on the equatorward flank of the subtropical winds in both hemispheres. This feature was also seen in the barotropic model and is associated with the strong easterlies in this latitude band predominantly during JJA (refer to Figure 8a). We have investigated these features further and have verified that low-latitude cyclonic wave breaking only occurs in sectors of the hemisphere where strong easterlies are present.

4.2. Influence of the Subtropical Jet in JJA

[37] It has been hypothesized that a strong subtropical jet prevails over the Indian and Pacific Oceans during JJA and can significantly reduce the positive eddy-mean flow feedback by influencing the location of wave breaking [*Eichelberger and Hartmann*, 2007; *Barnes and Hartmann*, 2010a, 2011]. Our algorithm allows us to determine whether the presence of these strong upper-level winds during winter modifies wave breaking distributions and potentially influences the eddy-mean flow feedbacks in the midlatitudes.

[38] To address this question, we calculate wave breaking frequencies analogous to those for the barotropic model (Figure 7) for Southern Hemisphere winter-time (JJA) wave breaking in ERA-Interim (Figure 9). With the results from the barotropic model as a guide, we begin by compositing wave breaking frequencies in a sector of the Indian Ocean basin (60°E–80°E) where both a strong subtropical and

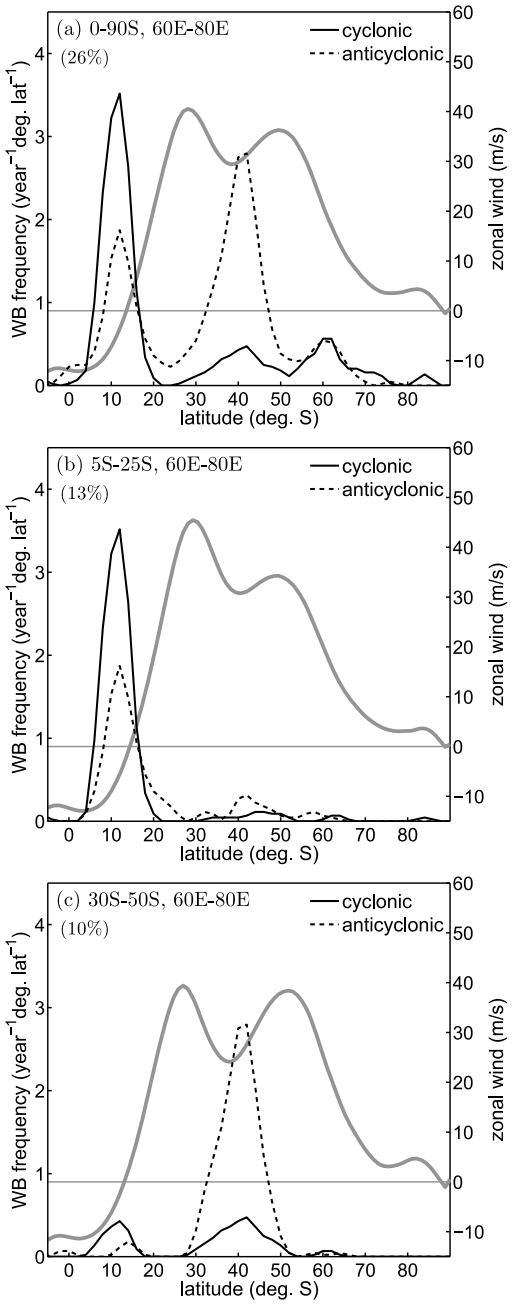

Figure 9. Wave breaking frequency versus latitude at 250 hPa from ERA-Interim during JJA. Frequencies are composited on days when there is a wave breaking event in the Indian Ocean sector (60°E–80°E) for various latitude bands. Black solid lines denote cyclonic wave breaking events and black dashed lines denote anticyclonic events. The gray solid curve denotes the total zonal-mean zonal wind in the specified sector composited on days when there is wave breaking there. The percentage of days within JJA with wave breaking in the specified sector is shown in the upper-left-hand corner of each panel.

eddy-driven jet are present during JJA. Note that similar conclusions are reached if one uses the South Pacific Ocean basin instead (not shown). Figure 9a shows composited wave breaking frequencies and zonal winds in this sector on days when there is a wave breaking event between 0°–90°S. In many respects, the observed Southern Hemisphere wave breaking profiles shown in Figure 9a are strikingly similar to the barotropic case with an imposed subtropical jet (Figure 7a). Both exhibit a double-peaked anticyclonic frequency distribution in the subtropics, one located on the flank of the subtropical winds, and the other on the apparent "flank" of the eddy-driven jet. In the observations, however, there is a much higher tendency for cyclonic wave breaking at low latitudes due to the enhanced easterlies in this region that are not present in the barotropic simulations with a subtropical jet.

[39] Figures 9b and 9c show additional composites for the Indian Ocean basin but split into days when wave breaking occurs on the flank of the subtropical jet (Figure 9b) and in the midlatitudes (Figure 9c). As seen in the barotropic simulations, waves break predominantly on the equatorward flank of the subtropical jet when the subtropical jet is much stronger than the eddy-driven jet. When the two jets become more separated, the eddy-driven jet is more likely to influence the location of wave breaking.

4.3. Comparison of Wave Breaking in Absolute and Potential Vorticity

[40] In the barotropic model with only a single surface, absolute vorticity is the obvious field on which to identify large-scale overturning. However, in diagnosing wave breaking in the observations, isentropic potential vorticity is the most frequently used field by virtue of its conservative properties. In this section we will demonstrate that use of absolute vorticity and isentropic potential vorticity yield similar wave breaking climatologies in the midlatitudes, while disparities in the tropics are likely due to differences in the heights of the relevant surfaces.

[41] We compare wave breaking frequencies of the 250 and 125 hPa absolute vorticity (η_{250} and η_{125}) and potential vorticity on the 350 K potential temperature surface (PV_{350K}) from ERA-Interim. We have chosen the 350 K surface because this surface has been cited to adequately represent wave breaking frequencies on nearby isentropic surfaces [*Strong and Magnusdottir*, 2008; *Wang and Magnusdottir*, 2011].

[42] The zonal-mean wave breaking frequency distributions for the three fields are plotted in Figure 10. To first order, the magnitudes of the wave breaking frequencies are similar for all fields, although there are more overturning

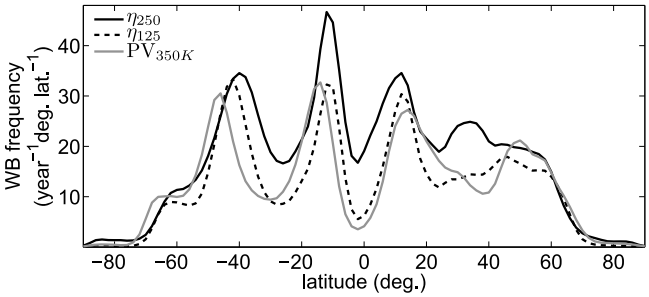

Figure 10. Meridional profiles of total wave breaking in ERA-Interim based on absolute vorticity on the 250 and 125 hPa surfaces (η_{250} and η_{125}) and potential vorticity on the 350 K potential temperature surface.

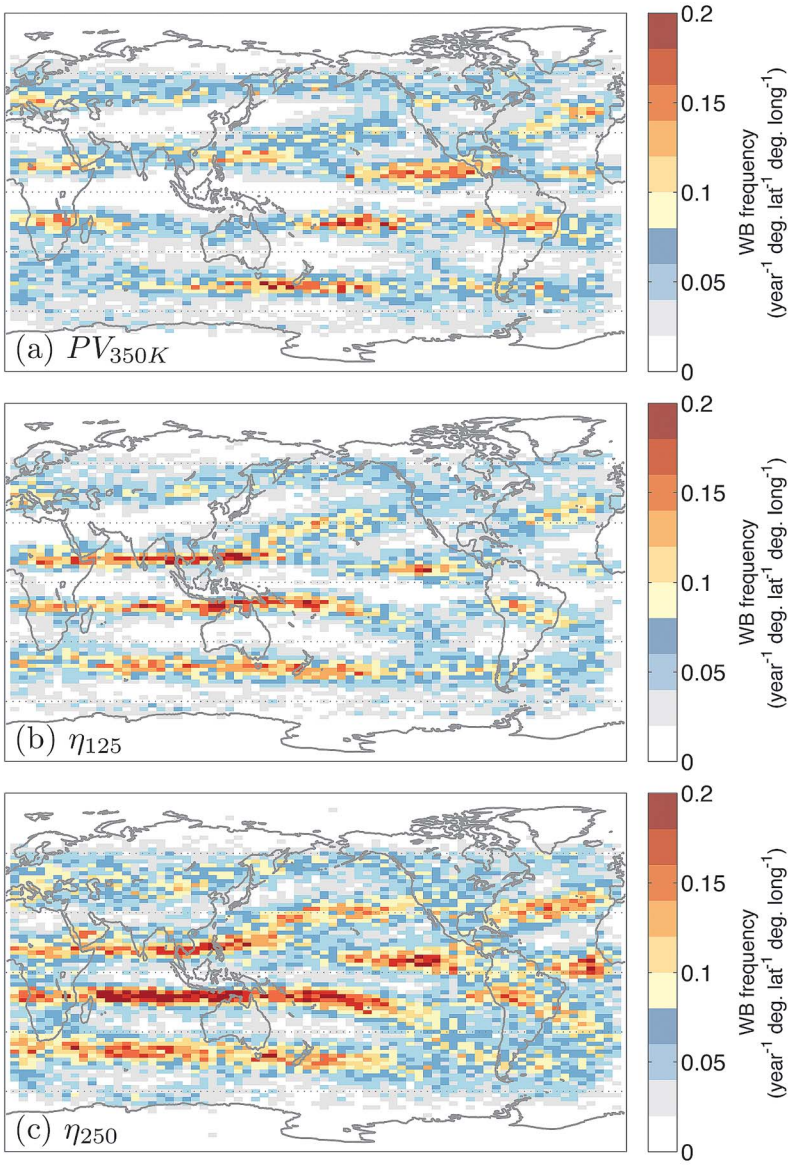

Figure 11. Latitude-longitude gridded wave breaking frequency in the annual mean from ERA-Interim based on (a) potential vorticity on the 350 K potential temperature surface, and absolute vorticity at (b) 125 hPa and (c) 250 hPa.

events identified by η_{250}. η_{125} compares very well with PV_{350K} likely because both surfaces are in close proximity to each other (refer to Figure 3), although there is an apparent poleward shift of the potential vorticity maxima. A likely reason for the small shift between the η_{125} and PV_{350K} distributions is that the centroid of each event is defined as the mean latitude of all overturning grid points. Since potential vorticity has a very large gradient in the subtropics, the more poleward contours are more likely to identify wave breaking and thus the centroids are more heavily weighted toward the pole. We have confirmed that this is the case by defining the latitude of an event as the latitude of the grid point closest to the pole. Using this definition, we find that the latitude of maximum midlatitude wave breaking agrees between all three curves to within 2.5° (not shown).

[43] The η_{250} shows significantly more tropical wave breaking compared to the other two curves. To demonstrate the reason, Figure 11 shows latitude-longitude frequency plots of wave breaking for PV_{350K}, η_{125} and η_{250}. The increased tropical wave breaking in η_{250} is not due to zonally symmetric tropical wave breaking, but rather predominantly occurs off of the Guinea Coast and in the equatorial eastern Pacific. These regions are known to be areas in the troposphere with westerlies along the equator, allowing Rossby waves to propagate from one hemisphere to another [*Webster and Holton*, 1982; *Waugh and Polvani*, 2000; *Barnes and Hartmann*, 2012]. These findings mimic those of Hitchman and Huesmann [2007] where enhanced tropical wave breaking was also found in regions of cross-equatorial flow. Equatorial westerlies are absent in the lower-

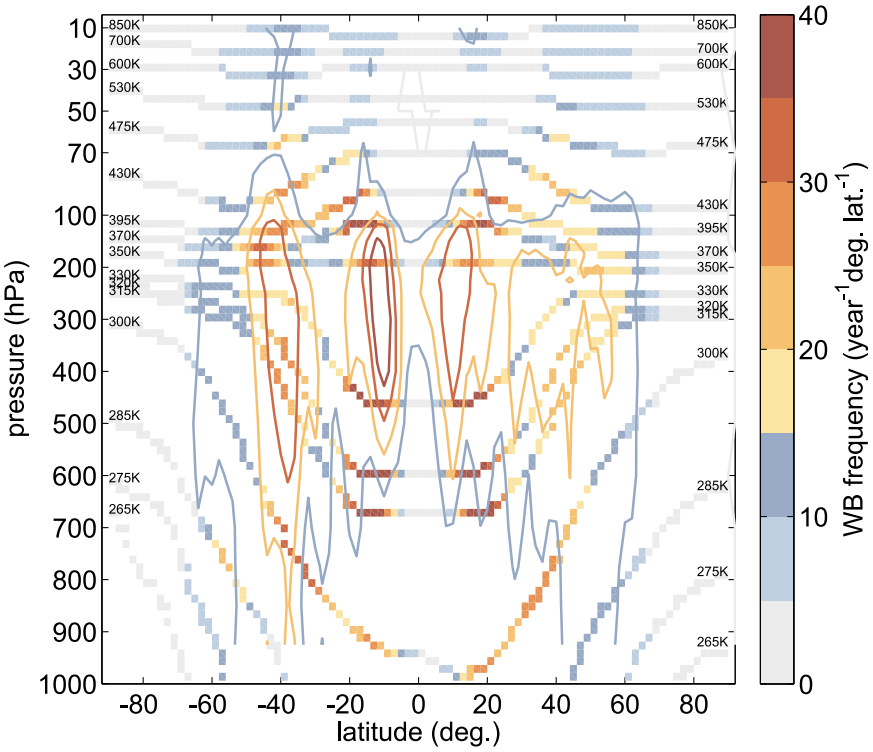

Figure 12. Annual mean, zonally integrated total wave breaking frequency for the ERA-Interim Reanalysis. Colored grid boxes denote frequencies calculated with isentropic potential vorticity and are plotted along their respective climatological potential temperature surfaces (see Figure 3). Contour lines denote wave breaking frequencies calculated using absolute vorticity on pressure surfaces.

stratosphere, and so η_{125} and PV_{350K} do not show large wave breaking frequencies there. In addition, it is possible that the waves breaking in these longitudinal bands did not propagate from midlatitudes, but rather were excited in situ by tropical convection [*Kiladis*, 1998].

[44] Perhaps it is not surprising that the potential vorticity-based method compares so well with that of absolute vorticity at levels where the isentropes coincide with pressure surfaces. *Baldwin and Holton* [1988] demonstrate that in the middle stratosphere, the PV on 850 K is well represented by the 10 hPa absolute vorticity and commented on its application to wave breaking diagnostics. It is less clear that this should be the case near the tropopause or in the troposphere, where the isentropes have substantial meridional slopes. In view of the barotropic structure of wave breaking [*Polvani and Saravanan*, 2000] and the fact that we are interested in wave breaking on large scales, it seems that absolute vorticity on pressure surfaces is capable of capturing the general distribution of wave breaking frequency.

[45] To further justify the use of isobaric absolute vorticity instead of isentropic potential vorticity, Figure 12 compares the annual-mean, zonally integrated wave breaking frequencies calculated using each method. In the figure, the colored grid boxes denote frequencies calculated using isentropic potential vorticity and are plotted along their respective climatological potential temperature surfaces as shown in Figure 3. The colored contours denote wave breaking frequencies from isobaric absolute vorticity and are equivalent to the frequencies plotted in Figures 8a and 8b but for the annual mean. Overall, isobaric absolute vorticity and isentropic potential vorticity exhibit very similar wave breaking frequencies. The wave breaking distributions in the stratosphere are nearly identical, which is perhaps not surprising considering that the isentropes align with pressure surfaces at these levels. Differences arise below about 500 hPa, where isentropic potential vorticity identifies more wave breaking events than absolute vorticity. However, both methods identify similar peaks in wave breaking frequency near 15°S, 40°S and 10°N.

[46] Our ultimate goal is to quantify the effect of jet latitude on wave breaking in the observations and to understand how wave breaking frequency might change with increased greenhouse gas emissions. Isentropic potential vorticity is rarely available in GCM output, and so absolute vorticity on pressure surfaces has the added benefit of being easily computed from the horizontal wind fields. For all of these reasons, we shall use the absolute vorticity field on isobaric surfaces to identify large-scale wave breaking in the reanalysis and GCMs from this point on.

5. Response of Wave Breaking to Climate Change

[47] One of the most robust responses of the circulation to increased greenhouse gas concentrations is a poleward shift of the midlatitude jet streams [*Trenberth et al.*, 2007]. In the annual mean, the reanalysis places the Southern Hemisphere eddy-driven jet at 52°S. Thus, results from the barotropic model suggest that a poleward shift of the jet stream could cause a reduction in cyclonic wave breaking events on the poleward flank of the jet. In addition, if barotropic dynamics

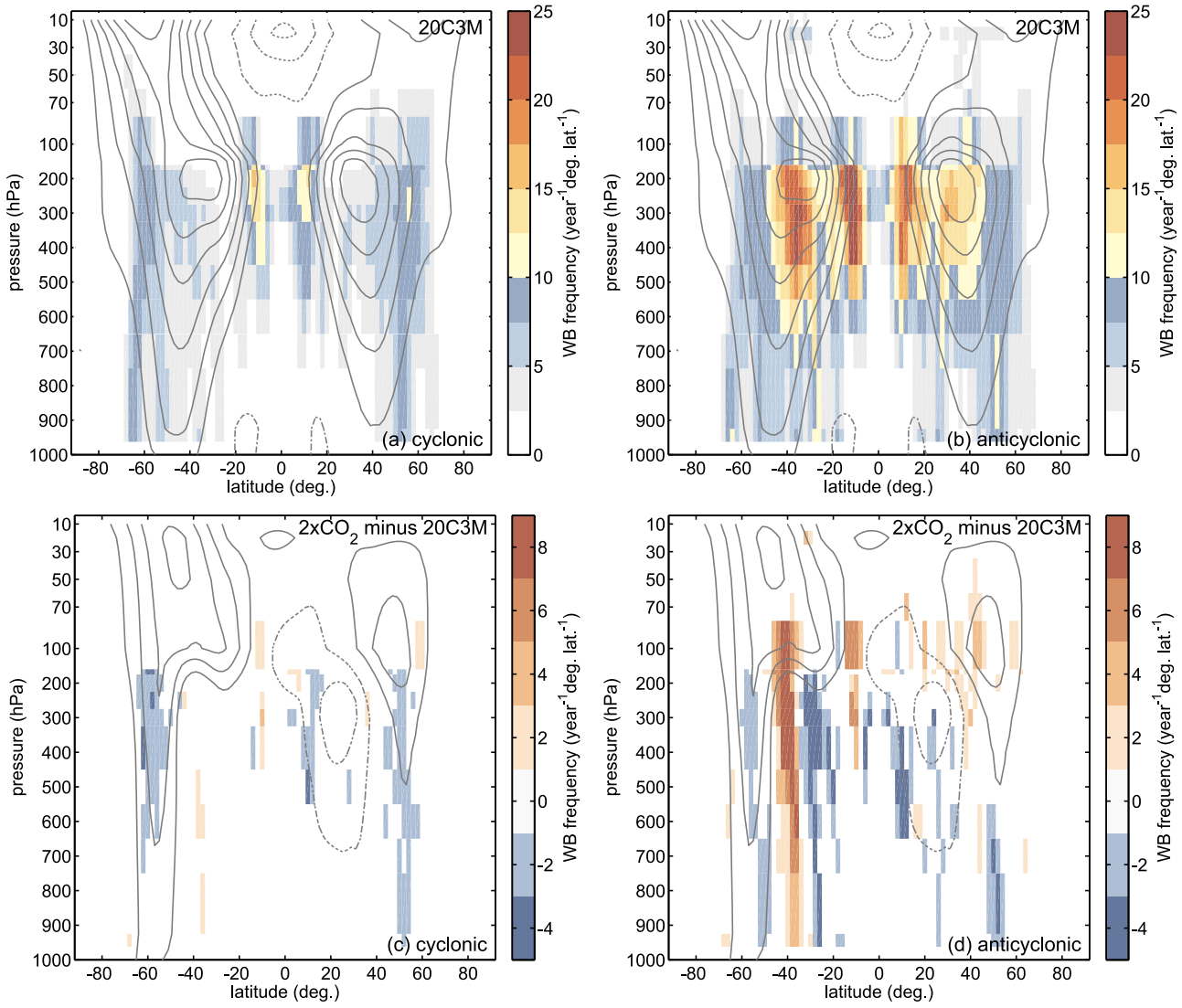

Figure 13. Zonally integrated wave breaking frequency for the GFDL CM2.0 model. (a) Cyclonic and (b) anticyclonic wave breaking frequency for the 20C3M (1961–2000) integration and (c, d) the difference in wave breaking frequency between the 2 × CO_2 and 20C3M integrations, where only statistically significant changes are shaded (see Appendix A for details). Gray contours denote the zonal-mean zonal winds contoured every 5 m/s (Figures 13a and 13b), and change in the winds between the 2 × CO_2 and 20C3M integrations contoured every 2 m/s with the zero lines omitted (Figures 13c and 13d). Dashed gray lines denote easterlies, and the linear vertical spacing changes at 100 hPa to highlight the stratosphere.

are relevant for the observed atmosphere, Figure 6 suggests that the anticyclonic wave breaking will shift poleward with the jet while the cyclonic wave breaking maximum might not as it may already have reached its poleward limit. To diagnose changes in wave breaking with climate change, we first present results from a single GCM before presenting results for all other models.

5.1. Wave Breaking in a Single GCM

[48] The wave breaking frequency distribution for the 20C3M integration of the GFDL CM2.0 model is shown in Figures 13a and 13b. There are fewer wave breaking events in the stratosphere in the GCM compared to the observations (Figures 8c and 8d), perhaps due to the model's limited vertical resolution. Although the GCM exhibits local maxima in wave breaking on the flanks of the eddy-driven and subtropical jet as in the observations, the frequency of both cyclonic and anticyclonic wave breaking events is not as large as observed.

[49] We calculated the wave breaking frequency distribution for the 2 × CO_2 scenario and plot the difference from the 20C3M integration in Figures 13c and 13d. Only differences that are statistically different from zero at 95% confidence based on the criterion from Appendix A are shaded. Referring first to the anticyclonic events (Figure 13d), anticyclonic wave breaking clearly shifts in the Southern Hemisphere as the jet shifts poleward by approximately 3.75°. A small shift also appears in the Northern Hemisphere, although the signal is not as clear. In addition, anticyclonic wave breaking events extend upward in both hemispheres, and we speculate that

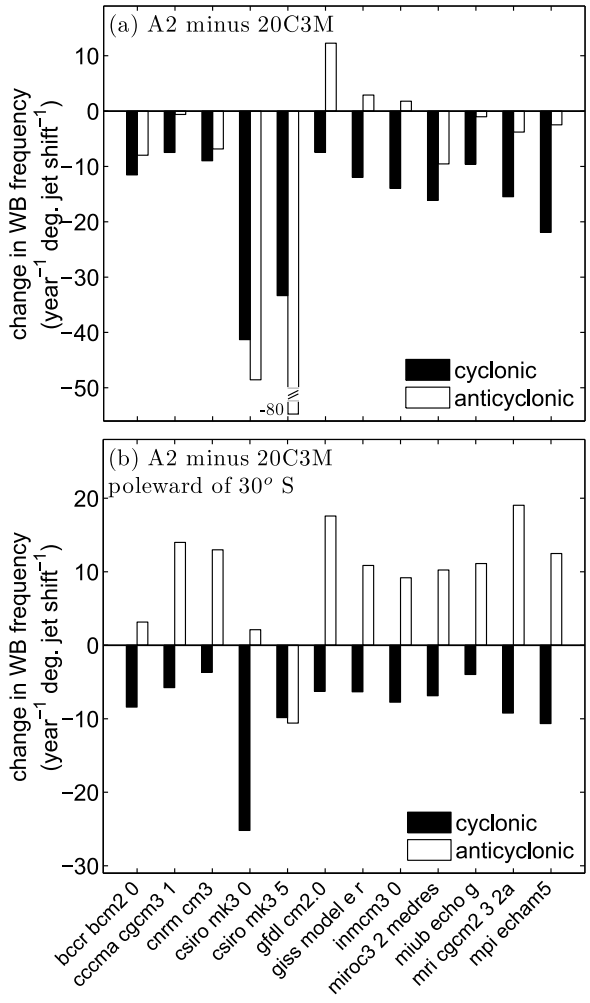

Figure 14. (a) Change in the number of Southern Hemisphere wave breaking events at 250 hPa per year per degree poleward shift of the jet between the A2 (2081–2100) and 20C3M (1961–2000) integrations for 12 CMIP3 GCMs. (b) Same as in Figure 14a except only for latitudes poleward of 30°S.

this is linked to a rising of the tropopause as the climate warms. Note that by identifying wave breaking on pressure surfaces, we are able to diagnose vertical displacements of wave breaking with an upward shift of the tropopause in pressure with climate change assuming multiple pressure levels are studied. An algorithm searching for wave breaking on the dynamic tropopause would not see such a shift because the contour would move upward with the tropopause by definition.

[50] Turning our attention to cyclonic wave breaking events (Figure 13c), cyclonic wave breaking decreases in both hemispheres by up to 30% at the latitude of maximum zonal wind anomalies with a doubling of carbon dioxide. However, in contrast to the change in anticyclonic events, this reduction is not accompanied by an increase farther poleward. Thus, consistent with the barotropic model results, a poleward shift of the jet is accompanied by a hemispheric decrease in cyclonic wave breaking frequency. The GFDL model exhibits a decrease of approximately 10 cyclonic wave breaking events per year per degree poleward shift of the jet, whereas the barotropic model integrations with midlatitude stirring exhibit a decrease of approximately 15 cyclonic wave breaking events per year per degree poleward shift of the jet. This comparison supports the notion that the barotropic effect of jet latitude on wave breaking might also be relevant in more realistic atmospheres.

5.2. Wave Breaking in the CMIP3 Models

[51] Now that we have presented detailed wave breaking distributions for a single GCM, we present a summary of results for all of the available CMIP3 models for two scenarios (20C3M and A2). We define the latitude of the eddy-driven jet as the latitude of maximum zonal-mean zonal wind at 925 hPa. Results are similar if the latitude of maximum surface westerlies is used instead.

[52] The calculated change in 250 hPa Southern Hemisphere wave breaking frequency between the A2 and 20C3M scenarios is plotted in Figure 14a for the 12 models with available data. We have scaled the change in wave breaking by the magnitude of the jet shift between model integrations to produce a change per degree latitude shift of the jet. Anticyclonic wave breaking increases in some models and decreases in others. However, cyclonic wave breaking decreases in all models, and in 10 of the 12 models, the rate of decrease falls between 7 and 20 events per year per degree shift, similar to the slopes calculated from the barotropic integrations. In terms of the percentage change, this corresponds to a total decrease in cyclonic wave breaking between 3.5% to 11% in the hemispheric mean, with local decreases of over 30% in some models. These results once again suggest that cyclonic wave breaking frequency is tied to the latitude of the midlatitude jet, and that it will decrease if the jets shift poleward with climate change.

[53] The varying response of anticyclonic wave breaking frequencies is largely a function of the latitude band over which one averages. Poleward of 30°S, all but one model shows an increase in anticyclonic wave breaking as shown in Figure 14b, while all models show a decrease in anticyclonic wave breaking between 0°–30°S (not shown). Thus, when the total change in anticyclonic wave breaking is averaged over the hemisphere, the result is the difference between two large numbers. It is possible that the decrease in anticyclonic wave breaking in the tropics and subtropics shown here is due to the rising of the tropopause, such that the 250 hPa surface falls below the level of maximum wave breaking frequency in the A2 integrations. However, additional calculations of wave breaking on nearby pressure surfaces are required to confirm that this is the case since other factors such as changes in the location of the subtropical jet may also be important.

[54] To determine how the latitudes of wave breaking shift with the climatological jet, we calculate the latitudes of maximum cyclonic and anticyclonic wave breaking for each integration. Details of this calculation are given in Appendix B. Figure 15 shows the latitudes of maximum cyclonic and anticyclonic wave breaking across all models and forcing scenarios. As is the case for the barotropic model, we see that the peak in anticyclonic wave breaking always occurs equatorward of the eddy-driven jet, while the peak in cyclonic wave breaking tends to be found poleward

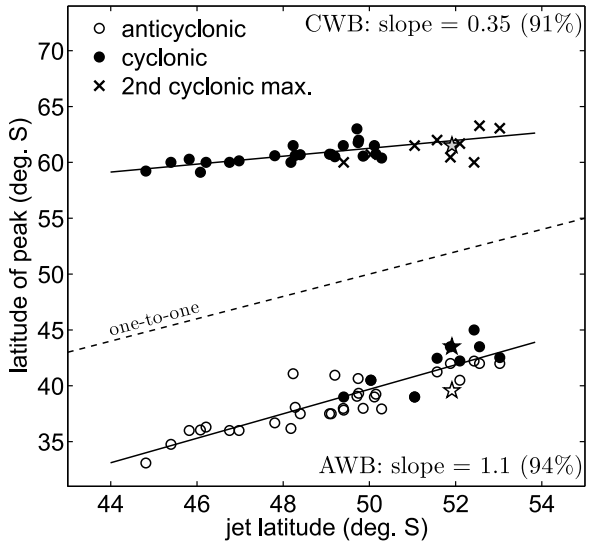

Figure 15. Latitude of maximum midlatitude wave breaking versus the latitude of the eddy-driven jet in the CMIP3 GCMs. Crosses denote the secondary maxima of cyclonic wave breaking when a double peaked distribution exists. ERA-Interim results are plotted as stars, with the gray star denoting the secondary cyclonic maximum. The solid lines denote the orthogonal-least squares fit for anticyclonic and the most poleward cyclonic wave breaking peaks, with the slope and percent variance explained displayed as text. The dashed line is the one-to-one line.

of the jet. However, in six of the integrations, the maximum cyclonic wave breaking occurs equatorward of the jet, with a secondary maximum located on the poleward flank which we denote by a cross. A similar result was obtained in the barotropic model, where the maximum cyclonic wave breaking could no longer shift poleward, and instead moved to the equatorward flank of the jet. The GCMs in which this occurs are the ones with jets nearest the pole, and so it is likely the barotropic and GCM integrations are both exhibiting related phenomena.

[55] While the majority of models place the jet equatorward of the jet in the reanalysis, Figure 15 shows that the observed latitudes of maximum cyclonic (black star) and anticyclonic (white star) wave breaking align well with those in the GCMs whose jet location matches the observations. In addition, the majority of observed cyclonic wave breaking occurs *equatorward* of the jet, with a secondary maximum on the poleward flank (gray star), consistent with the behavior of the GCM integrations with similar jet latitudes.

[56] Figure 15 shows that as the eddy-driven jet is found further poleward, the peak anticyclonic wave breaking also shifts toward the pole. We calculate the orthogonal least squares best fit for the anticyclonic events, and display the percent variance explained and slope in the bottom right corner of the figure. The best fit line has a slope of 1.1 degree shift of wave breaking per degree shift of the jet, where a slope of 1 implies that the wave breaking shifts exactly with the jet. A similar line is fit to the poleward cyclonic maximum, where secondary maxima are included (although results are similar if they are not). In this case, the resulting slope is only 0.35, implying that for every degree shift of the jet, the cyclonic wave breaking on the poleward flank shifts by less than half as much.

[57] These results are generally consistent with those from the barotropic model: jets poleward of 50° latitude have maximum cyclonic wave breaking on their equatorward flanks, demonstrating that a poleward shift of the eddy-driven jet does not necessarily imply an equivalent shift in the latitudes of upper-level wave breaking. These results support the idea that there is a limit to how far poleward wave breaking can shift with the jet.

[58] Interestingly, *Rivière* [2011] diagnosed wave breaking of absolute vorticity on the 200 hPa surface in two of the CMIP3 models and also found a decrease in cyclonic wave breaking when the jet shifts poleward. However, a direct comparison with their results is difficult, as their wave breaking profiles differ greatly from those shown here and do not detect a maximum in wave breaking on the equatorward flanks of the subtropical jets. This difference may be due to the fact that their algorithm does not count distinct events, but rather includes all grid points where overturning is taking place.

6. Conclusions

[59] Wave breaking is identified in a barotropic model, reanalysis data set and in data from 13 general circulation models (GCMs). Results obtained using isentropic potential vorticity compare well with those obtained using absolute vorticity on pressure surfaces, both showing maximum wave breaking frequencies on the equatorward flanks of the midlatitude and subtropical jets. We demonstrate that a poleward shift of the climatological midlatitude jet causes a reduction in cyclonic wave breaking on the jet's poleward flank, and we attribute this decrease to the disappearance of the critical line near the pole. We also demonstrate a poleward limit to the location of maximum cyclonic wave breaking and show evidence that the observed Southern Hemisphere circulation may have already reached this limit. These GCM results suggest that cyclonic wave breaking frequency could decrease by up to 11% in the hemispheric mean with a poleward shift of the midlatitude jet between the A2 (2081–2100) and 20C3M (1961–2000) integrations.

[60] Consistent with our findings, *Rivière et al.* [2010] detected wave breaking of absolute vorticity on the 200 hPa surface in present-day and last-glacial maximum GCM simulations and found that cyclonic wave breaking frequency increases and anticyclonic wave breaking decreases when the jet is further equatorward. *Rivière* [2009] and *Rivière et al.* [2010] explain the influence of jet latitude on wave breaking frequency by the competing effects of the absolute vorticity gradient and the stretching term in the potential vorticity gradient which promote anticyclonic and cyclonic wave breaking respectively. However, the barotropic model in the present study is nondivergent (no stretching term) and we still find a significant influence of jet latitude on wave breaking orientation similar to what is found in the GCMs and observations, suggesting that the absolute vorticity gradient is the dominant controller.

[61] Wave breaking by definition is an irreversible process. Although our algorithm classifies waves that are in the process of overturning, it does not guarantee that irreversible mixing has or will occur. In the past, studies have addressed

this by only identifying potential vorticity streamers that are nearly cut off from their stratospheric source [*Martius et al.*, 2007]; however, further work is required to determine the extent to which these two methods differ.

[62] This work highlights the importance of understanding the response of the background flow to predicting how both high- and low-latitude wave breaking will respond to a changing climate. A decrease in high-latitude wave breaking could mean a decrease in blocking anticyclone frequency due to the strong relationship between the two [*Woollings et al.*, 2008]. Indeed, recent results show that blocking frequency decreases in most of the CMIP3 models over the next century, where models with larger poleward jet shifts exhibit larger decreases [*Barnes and Hartmann*, 2010b; *Barnes et al.*, 2012]. At low latitudes, changes in the subtropical winds have the potential to move wave breaking to higher altitudes and potentially influence the wave driving of the stratospheric circulation [*Shepherd and McLandress*, 2011].

Appendix A: Statistical Significance of Changes in Wave Breaking Frequency

[63] We determine the statistical significance of the change in wave breaking frequency between the 2 × CO_2 and 20C3M scenarios by first assuming that within each integration, the underlying frequencies do not vary over time. We test whether changes in the time mean, zonally integrated wave breaking onset frequency ($\overline{X}$) at a given latitude and pressure are statistically different from zero between the 2 × CO_2 ($\overline{X}_{2\times}$) and 20C3M ($\overline{X}_{20C3M}$) integrations.

[64] At each time (t), pressure (p), latitude (θ) and longitude (λ), let $B(t, p, \theta, \lambda) = 1$ when there is a wave breaking event and = 0 when there is not. Then $\overline{X}$ at p and θ is simply the temporal average of $X(t, p, \theta) = \sum_\lambda B(t, p, \theta, \lambda)$ over the duration of the data set. To calculate the confidence of $\overline{X}$ and its deviation from a corresponding value in another system, we must estimate the variance of $\overline{X}$ that results from the finiteness of the sample used to estimate it. When estimating this variance it is necessary to take into account temporal correlations in $X(t, p, \theta)$, correlations which follow from temporal correlations in $B(t, p, \theta, \lambda)$ since a given event can last multiple days making it impossible for another event to occur there until the first is complete.

[65] To calculate the confidence bounds on the mean of $X(t) = \overline{X}$, we must estimate the variance of $\overline{X}$, which is likely to be influenced by the temporal correlations of the $X(t)$s. Section 2.1.5 of *Box et al.* [2008] provides a complete discussion of this standard time series problem.

[66] The general form of the variance of $\overline{X}$ can be computed and becomes

$$\mathbf{Var}(\overline{X}) = \mathbf{Var}\left(\frac{1}{N}\sum_{t=1}^{N} X(t)\right) = \frac{\sigma^2}{N^2}\sum_{s=1}^{N}\sum_{t=1}^{N}\rho_{|t-s|}, \qquad \text{(A1)}$$

where N is the length of the time series, $\sigma^2 = \mathbf{Var}(X(t))$ and ρ_h is the autocorrelation of $X(t)$ at lag h.

[67] Defining $\overline{\rho}$ as

$$\overline{\rho} = \frac{1}{N^2}\sum_{s=1}^{N}\sum_{t=1}^{N}\rho_{|t-s|} = \frac{1}{N^2}\left[N + 2\sum_{h=1}^{N-1}(N-h)\rho_h\right], \qquad \text{(A2)}$$

we can write that

$$\mathbf{Var}(\overline{X}) = \sigma^2\overline{\rho}. \qquad \text{(A3)}$$

[68] To estimate the variance σ^2, we begin with the sample variance S^2 of the observed temporally correlated $X(t)$'s:

$$S^2 = \frac{1}{N-1}\sum_{t=1}^{N}(X(t) - \overline{X})^2. \qquad \text{(A4)}$$

Manipulating this equation, utilizing (A3), and requiring N to be large results in

$$\sigma^2 \approx \frac{S^2}{1-\overline{\rho}}. \qquad \text{(A5)}$$

[69] Thus, substituting back into (A3) leads to

$$\mathbf{Var}(\overline{X}) \approx S^2\frac{\overline{\rho}}{1-\overline{\rho}}. \qquad \text{(A6)}$$

The formula for $\overline{\rho}$ tells us that if the autocorrelation drops to zero for $h > 0$, then $\overline{\rho} = 1/N$ and we obtain the usual estimate for the variance of the mean ($S^2 \cdot N^{-1}$).

[70] For large N, $\overline{X}$ is well modeled by the Normal distribution, and thus the difference between $\overline{X}_{2\times}$ and $\overline{X}_{20C3M}$ is also normal. Thus, our test statistic z is defined at each latitude and pressure and follows a Standard Normal distribution, where z is defined as

$$z = \frac{\overline{X}_{2\times} - \overline{X}_{20C3M}}{\sqrt{\mathbf{Var}(\overline{X}_{2\times}) + \mathbf{Var}(\overline{X}_{20C3M})}}. \qquad \text{(A7)}$$

[71] Calculating the relevant values for the 2 × CO_2 and 20C3M scenarios for each latitude-longitude bin, plugging them in and requiring 95% confidence leads to the significant differences that are shaded in Figures 13c and 13d.

Appendix B: Calculation of the Latitude of Peak Wave Breaking Frequency

[72] The latitude of peak wave breaking is defined by binning the zonally integrated wave breaking events into 1.5° latitude bins and then applying a 1-2-1 filter twice. All local maxima of the frequency distribution are found, and the most poleward maximum in midlatitude anticyclonic wave breaking (equatorward of 55°) defines the anticyclonic peak latitude. We look equatorward of 55° to ensure that small local maxima at high latitudes are not identified. In some cases, the peak in anticyclonic wave breaking near the equator is larger than in midlatitudes, so we look for the most poleward peak to ensure that we identify the maximum associated with the flank of the eddy-driven jet.

[73] To calculate the peak latitudes of cyclonic wave breaking events, we find the most poleward local maximum between 20° and 70°. In many instances, cyclonic wave breaking has a bimodal distribution in the mid- to high-latitudes. When the more equatorward peak is larger in magnitude, we identify both peaks as locations of maximum cyclonic wave breaking and the more poleward (smaller in magnitude) is plotted as a cross in Figure 6.

[74] **Acknowledgments.** We wish to first thank Olivia Martius, Courtenay Strong and one anonymous reviewer for their thorough comments on an earlier version of this manuscript. Thank you also to Darryn Waugh and Lorenzo Polvani for their thoughts on previous work which lead the authors to develop this wave breaking algorithm. This work supported by the Climate Dynamics Program of the National Science Foundation under grant AGS-0960497. The ERA-Interim global atmospheric reanalysis has been provided by ECMWF and is distributed by the Computational Information and Systems Laboratory (CISL) at the National Center for Atmospheric Research (NCAR). We acknowledge the modeling groups, the Program for Climate Model Diagnosis and Intercomparison (PCMDI) and the WCRP's Working Group on Coupled Modeling (WGCM) for their roles in making available the WCRP CMIP3 multimodel data set. Support of this data set is provided by the Office of Science, U.S. Department of Energy.

References

Abatzoglou, J. T., and G. Magnusdottir (2007), Wave breaking along the stratospheric polar vortex as seen in ERA-40 data, *Geophys. Res. Lett.*, *34*, L08812, doi:10.1029/2007GL029509.

Baldwin, M. P., and J. R. Holton (1988), Climatology of the stratospheric polar vortex and planetary wave breaking, *J. Atmos. Sci.*, *45*, 1123–1142.

Barnes, E. A., and D. L. Hartmann (2010a), Dynamical feedbacks of the Southern Annular Mode in winter and summer, *J. Atmos. Sci.*, *67*, 2320–2330.

Barnes, E. A., and D. L. Hartmann (2010b), Influence of eddy-driven jet latitude on North Atlantic jet persistence and blocking frequency in CMIP3 integrations, *Geophys. Res. Lett.*, *37*, L23802, doi:10.1029/2010GL045700.

Barnes, E. A., and D. L. Hartmann (2011), Rossby-wave scales, propagation and the variability of eddy-driven jets, *J. Atmos. Sci.*, *68*, 2893–2908.

Barnes, E. A., and D. L. Hartmann (2012), The global distribution of atmospheric eddy-length scales, *J. Clim.*, in press.

Barnes, E. A., D. L. Hartmann, D. M. W. Frierson, and J. Kidston (2010), The effect of latitude on the persistence of eddy-driven jets, *Geophys. Res. Lett.*, *37*, L11804, doi:10.1029/2010GL043199.

Barnes, E. A., J. Slingo, and T. Woollings (2012), A methodology for the comparison of blocking climatologies across indices, models and climate scenarios, *Clim. Dyn.*, doi:10.1007/s00382-011-1243-6, in press.

Box, G. E. P., G. M. Jenkins, and G. C. Reinsel (2008), *Time Series Analysis: Forecasting and Control*, 4th ed., 746 pp., John Wiley, Hoboken, N. J.

Delworth, T., et al. (2006), GFDL's CM2 global coupled climate models - Part 1: Formulation and simulation characteristics, *J. Clim.*, *19*, 643–674.

Edmon, H. J., B. J. Hoskins, and M. E. McIntyre (1980), Eliassen-Palm cross sections for the troposphere, *J. Atmos. Sci.*, *37*, 2600–2615.

Eichelberger, S. J., and D. L. Hartmann (2007), Zonal jet structure and the leading mode of variability, *J. Clim.*, *20*, 5149–5163, doi:10.1175/JCLI4279.1.

Held, I. M. (1983), Stationary and quasi-stationary eddies in the extratropical troposphere: Theory, in *Large-Scale Dynamical Processes in the Atmosphere*, edited by B. J. Hoskins and R. P. Pearce, pp. 127–168, Academic, London.

Hitchman, M. H., and A. S. Huesmann (2007), A seasonal climatology of Rossby wave breaking in the 320-2000-K layer, *J. Atmos. Sci.*, *64*, 1922–1940.

Hoskins, B. J., and D. J. Karoly (1981), The steady linear response of a spherical atmosphere to thermal and orographic forcing, *J. Atmos. Sci.*, *38*, 1179–1196.

Hoskins, B. J., A. J. Simmons, and D. G. Andrews (1977), Energy dispersion in a barotropic atmosphere, *Q. J. R. Meteorol. Soc.*, *103*, 553–567.

Isotta, F., O. Martius, M. Sprenger, and C. Schwierz (2008), Long-term trends of synoptic-scale breaking Rossby waves in the Northern Hemisphere between 1958 and 2001, *Int. J. Climatol.*, *28*, 1551–1562, doi:10.1002/joc.1647.

Kiladis, G. (1998), Observations of Rossby waves linked to convection over the Eastern Tropical Pacific, *J. Atmos. Sci.*, *55*, 321–339.

Martius, O., C. Schwierz, and H. Davies (2007), Breaking waves at the tropopause in the wintertime Northern Hemisphere: Climatological analyses of the orientation and the theoretical LC1/2 classification, *J. Atmos. Sci.*, *64*, 2576–2592.

McIntyre, M. E., and T. N. Palmer (1983), Breaking planetary waves in the stratosphere, *Nature*, *305*, 593–600.

Meehl, G. A., C. Covey, T. Delworth, M. Latif, B. McAvaney, J. F. B. Mitchell, R. J. Stouffer, and K. E. Taylor (2007a), The WRCP CMIP3 multi-model dataset: A new era in climate change research, *Bull. Am. Meteorol. Soc.*, *88*, 1383–1394.

Meehl, G. A., et al. (2007b), Global climate projections, in *Climate Change 2007: The Physical Science Basis. Contribution of Working Group I to the Fourth Assessment Report of the Intergovernmental Panel on Climate Change*, pp. SM10.1–SM10.8, Cambridge Univ. Press, Cambridge, U. K.

Nakamura, M., and R. A. Plumb (1994), The effects of flow asymmetry on the direction of Rossby wave breaking, *J. Atmos. Sci.*, *51*, 2031–2045.

Ndarana, T., and D. W. Waugh (2011), A climatology of Rossby wave breaking on the Southern Hemipshere tropopause, *J. Atmos. Sci.*, *68*, 798–811, doi:10.1175/2010JAS3460.1.

Peters, D., and D. W. Waugh (1996), Influence of barotropic shear on the poleward advection of upper-tropospheric air, *J. Atmos. Sci.*, *53*, 3013–3031.

Polvani, L. M., and R. Saravanan (2000), The three-dimensional structure of Rossby waves in the polar wintertime stratosphere, *J. Atmos. Sci.*, *57*, 3663–3685.

Randel, W., and I. Held (1991), Phase speed spectra of transient eddy fluxes and critical layer absorption, *J. Atmos. Sci.*, *48*(5), 688–697.

Rivière, G. (2009), Effect of latitudinal variations in low-level baroclinicity on eddy life cycles and upper-tropospheric wave-breaking processes, *J. Atmos. Sci.*, *66*, 1569–1592.

Rivière, G. (2011), A dynamical interpretation of the poleward shift of the jet streams in global warming scenarios, *J. Atmos. Sci.*, *68*, 1253–1272.

Rivière, G., A. Laîné, G. Lapeyre, D. Salas-Mélia, and M. Kageyama (2010), Links between Rossby wave breaking and the North Atlantic Oscillation–Arctic Oscillation in present-day and Last Glacial Maximum climate simulations, *J. Clim.*, *23*, 2987–3008.

Robinson, W. A. (2006), On the self-maintenance of midlatitude jets, *J. Atmos. Sci.*, *63*, 2109–2122.

Shepherd, T. G., and C. McLandress (2011), A robust mechanism for the strengthening of the Brewer-Dobson Circulation in response to climate change: Critical-layer control of subtropical wave breaking, *J. Fluid Mech.*, *469*, 13–48.

Simmons, A., S. Uppala, D. Dee, and S. Kobayashi (2006), ERA-Interim: New ECMWF reanalysis products from 1989 onwards, *ECMWF Newsl.*, *110*, 25–35.

Strong, C., and G. Magnusdottir (2008), Tropospheric Rossby wave breaking and the NAO/NAM, *J. Atmos. Sci.*, *65*, 2861–2876, doi:10.1175/2008JAS2632.1.

Thorncroft, C. D., B. J. Hoskins, and M. E. McIntyre (1993), Two paradigms of baroclinic-wave life-cycle behaviour, *Q. J. R. Meteorol. Soc.*, *119*, 17–55.

Trenberth, K. E., et al. (2007), Observations: Surface and atmospheric climate change, in *Climate Change 2007: The Physical Science Basis. Contribution of Working Group I to the Fourth Assessment Report of the Intergovernmental Panel on Climate Change*, pp. 237–336, Cambridge Univ. Press, Cambridge, U. K.

Vallis, G. K., E. P. Gerber, P. J. Kushner, and B. A. Cash (2004), A mechanism and simple dynamical model of the North Atlantic Oscillation and annular modes, *J. Atmos. Sci.*, *61*, 264–280.

Wang, Y.-H., and G. Magnusdottir (2011), Tropospheric Rossby wave breaking and the SAM, *J. Clim.*, *24*, 2134–2146, doi:10.1175/2010JCLI4009.1.

Waugh, D., and L. Polvani (2000), Climatology of intrusions into the tropical upper troposphere, *Geophys. Res. Lett.*, *27*, 3857–3860.

Webster, P. J., and J. R. Holton (1982), Cross-equatorial response to middle-latitude forcing in a zonally varying basic state, *J. Atmos. Sci.*, *39*, 722–733.

Wernli, H., and M. Sprenger (2007), Identification and ERA-15 climatology of potential vorticity streamers and cutoffs near the extratropical tropopause, *J. Atmos. Sci.*, *64*, 1569–1580.

Woollings, T., B. Hoskins, M. Blackburn, and P. Berrisford (2008), A new Rossby wave-breaking interpretation of the North Atlantic Oscillation, *J. Atmos. Sci.*, *65*, 609–626.